Direct Numerical Simulation of Compressible Multiphase Flows:
Interaction of Shock Waves with Dispersed Multimaterial Media

Robert Nourgaliev[1], Nam Dinh[2], Theo Theofanous[3]

Center for Risk Studies and Safety, University of California, Santa Barbara, USA
1: robert@engineering.ucsb.edu 2: nam@engineering.ucsb.edu 3: theo@engineering.ucsb.edu

Abstract This paper is concerned with the direct numerical simulation of interactions, deformation and breakup of dispersed solid and fluid entities (bubbles, drops) in high-speed flows, e.g. under explosion and shock wave conditions. The challenge lies in the lack of an efficient approach to handle high-impedance interfaces with evolving topologies. We contribute a novel Eulerian-grid-based method named 'Characteristics-Based Matching' (CBM). Our basic idea is to respect information flow across multi-material interfaces within inherently transient and complex flow and pressure fields. We achieve this objective through a consistent use of numerical schemes based on Riemann-problem solutions in both single-fluid interior domains and two-fluid interfacial regions, so as to accurately account for complex interactions of shock and rarefaction waves with multimaterial interfaces. We bring to bear best features of front-tracking and front-capturing techniques, namely accuracy of interface advancement in the former and algorithmic simplicity of interface geometry treatment in the later. In the paper, we show that the CBM method is capable of providing accurate solutions for a number of challenging test problems of shocks interacting with compressible solid (copper), gas bubble, and stiff fluid (water) media.

1   Introduction and Background

Compressible multiphase flow is an area of emergent practical interest, particularly for the analysis of explosions and energetic dispersal of fluid and solid materials. The physics of such phenomena is complex. On the one hand, interactions of pressure waves with disperse entities significantly complicate flow structures; the shocks are transmitted and reflected multiple times across multi-material interfaces. On the other hand, such intense interactions may cause dispersed entities (particles, drops, bubbles) to deform and disintegrate. In this paper, we are concerned with capabilities to perform direct numerical simulation (DNS) for such flows. As discussed shortly below, while different numerical methods have been developed for DNS of multi-material flow, applications of existing methods to the flow situations of present interest are hampered by their inefficiency in dealing with evolving-topology interfaces and/or their inability to accurately capture dynamics of high-impedance interfaces. An approach to accurately handle high-impedance, complex-topology interfaces is needed and is the subject of this paper.

Existing methods for numerical simulation of multi-material flows can be categorized into three groups: Lagrangian (L), Arbitrary Lagrangian-Eulerian (ALE), and Eulerian (E). Each approach has its own pros and cons. The *Lagrangian* methods, which use moving with flow meshes, are in general considered to be the most accurate in the case of small deformation flows. However, they become highly complicated and less accurate, when applied to large displacement flows, due to inaccuracies and complexity of the mesh management when the mesh is periodically rezoned to eliminate large distortions of computational cells. The *Arbitrary Lagrangian-Eulerian* methods use Lagrangian formulation near the interface and moving-grid strategies with Eulerian schemes away from the interface. While the ALE methods allow to alleviate a problem with large deformation flows, attributed to the Lagrangian framework, they are still highly complicated in coding and low-accurate under large-deformation-flow conditions. Excellent reviews of Lagrangian and ALE methods are given by Benson (1992) and Mair (1999). The *Eulerian* methods use fixed grids and are relatively simple to

code. There are two classes of Eulerian methods, relative to their description of interface: the Front Tracking (FT) and Front Capturing (FC).

The *Front Tracking* methods use markers to describe interface. Each marker is propagated at each time step in a spatially operator-split manner, using a local coordinate system which is oriented normally to the interface. The normal propagation step is Riemann-solver-based, using an exact one-dimensional Riemann problem solution for conservation law with discontinuity. The tangential split steps utilize finite differences in a plane tangent to the interface. For details, see (Chern et al., 1985), (Cocchi and Saurel, 1997) and (Glimm et al., 1998). The FT methods are in general considered to be more accurate than the FC methods. The major drawback of these schemes is that they are very complex when extended to multi-dimensions.

Lately, the *Front Capturing* schemes become increasingly popular. In these methods, the interface is described by some scalar index function. Among the most popular index functions are the 'Level Set' (LS) function, the 'Volume-Of-Fluid' (VOF), the 'Mass Fraction' and the 'piecewise constant γ' function. An excellent review of FC methods can be found in the recent study by Abgrall and Karni (2001). The major advantage of the FC methods over the FT methods is their relative algorithmic simplicity to describe multi-dimensional complex-topology interfaces, including fragmentation, coalescence, immergence and disappearance of interfaces. However, in a frame of the *compressible multifluid dynamics*, they suffer from one very serious drawback, which only recently has started to be overcame. The Eulerian shock-capturing schemes always yield a numerical diffusion of discontinuities over a few computational nodes. This numerical diffusion is perfectly acceptable in single-fluid case. However, in multi-fluid flows, it is detrimental. Excellent examples of numerical failures are shown in (Abgrall, 1988), (Karni, 1996), (Fedkiw et al., 1999), and (Abgrall and Karni, 2001). The reason for this failure is the following. The numerical diffusion causes density to diffuse from one medium to another, generating a nonphysical zone, in which computation of pressure by any of two equations of state does not make any sense, since the equations of state are not continuous across the interface. The result is non-physical pressure oscillations, which are not the ones commonly associated with high-order schemes - they are present even for the first-order schemes. It is instructive to note that the FT methods do not suffer from this problem, because the interface is sharply resolved ("tracked"). The major breakthrough was made by Karni (1996), who realized that a strict conservation can be sacrificed for the sake of elimination of unphysical pressure oscillations. A number of different numerical schemes have been born, including (Karni, 1996), (Abgrall, 1996), (Fedkiw et al., 1999), (Saurel and Abgrall, 1999) and (Abgrall and Karni, 2001). All these schemes work very well for gas-gas (low-impedance-interface) flows and for one-dimensional gas-liquid flows. However, multidimensional high-impedance (gas/liquid and gas/solid) interface flows remain a serious challenge due to large sensitivity of the schemes to numerical errors across interfaces with a "stiff" equation of state (EOS) on either side.

In the present paper, we introduce a new Eulerian-grid-based method for the direct numerical simulation of compressible multi-material flow. The new method named Characteristics-Based Matching (CBM) leverages upon best features of the front-tracking and front-capturing techniques discussed above. We use a level-set method to handle topologically-complex multi-dimensional interfaces and a front-tracking-like method to accurately advance solution near the interface. Our main idea in this development is to respect information flow in such complex flow/pressure fields across multi-material interfaces. We achieve this objective by using the characteristics-based methods. In single-fluid interior domains, we use a high-order accurate Godunovs scheme based on the single-fluid Riemann solver. Near the interface, we employ a treatment based on the two-fluid Riemann problem solution. In the remaining of this paper, we provide details of the CBM method description and numerical im-

plementation and show calculational results which demonstrate the CBM method performance and discuss insights gained from a CBM study of a shock wave-liquid drop interaction.

2 Governing Equations

The governing equations of compressible fluid dynamics can be written in the following generic form:

$$\mathbf{U}_t + \left[\vec{\mathcal{F}}(\mathbf{U})\right]_x + \left[\vec{\mathcal{G}}(\mathbf{U})\right]_y + \left[\vec{\mathcal{H}}(\mathbf{U})\right]_z = 0 \tag{1}$$

where t is time; $\mathbf{x} = (x, y, z)$ is a position-vector; $\mathbf{U} = (\mathrm{U}_1, ..., \mathrm{U}_q)^{\mathsf{T}}$ and $(\vec{\mathcal{F}}, \vec{\mathcal{G}}, \vec{\mathcal{H}})$ are the vector of the conservation variables and the vector of physical fluxes in x, y and z directions respectively:

$$
\begin{aligned}
\mathbf{U} &= \begin{pmatrix} \rho \\ \rho u \\ \rho v \\ \rho w \\ \rho e \end{pmatrix}, &
\vec{\mathcal{F}} &= \begin{pmatrix} \rho u \\ P + \rho u^2 \\ \rho uv \\ \rho uw \\ u(P + \rho e) \end{pmatrix} \\
\vec{\mathcal{G}} &= \begin{pmatrix} \rho v \\ \rho vu \\ P + \rho v^2 \\ \rho vw \\ v(P + \rho e) \end{pmatrix}, &
\vec{\mathcal{H}} &= \begin{pmatrix} \rho w \\ \rho wu \\ \rho wv \\ P + \rho w^2 \\ w(P + \rho e) \end{pmatrix}
\end{aligned}
\tag{2}
$$

and q is a total number of the conservation variables. The Jacobian matrices $\mathbb{A}^{(x)} = \partial\vec{\mathcal{F}}/\partial\mathbf{U}$, $\mathbb{A}^{(y)} = \partial\vec{\mathcal{G}}/\partial\mathbf{U}$ and $\mathbb{A}^{(z)} = \partial\vec{\mathcal{H}}/\partial\mathbf{U}$ have q real eigenvalues and a complete set of eigenvectors. Here, ρ, P, $\mathbf{u} = (u, v, w)$ and e are the fluid density, static pressure, velocity vector and total specific energy, respectively.

In the present study, we will use the *stiffened gas equation of state* (Godunov et al., 1976), which can be written as

$$P = (\gamma - 1)\rho i - \gamma\Pi \tag{3}$$

where i is a specific internal energy, while the constants γ and Π are parameters characteristic of the material. This equation of state is a simple generalization of the ideal gas law equation of state, which provides a reasonable approximation of thermodynamic processes in gases, liquids and also in metals under high pressure conditions. The values of parameters γ and Π for some gases, liquids and solids are given in (Saurel and Abgrall, 1999).

3 Numerical Approach

In the present section, we will describe the numerical approach utilized in the present paper. First, the basic numerical scheme used to solve gas dynamics equations (1)-(3) inside each fluid will be presented in section 3.1. Then, the level set (LS) method used for interface capturing and a novel coupling boundary condition treatment (the Characteristics-Based Matching, CBM) will be introduced in sections 3.2 and 3.3, correspondingly.

3.1 Basic Numerical Scheme

Time discretization. For time discretization of governing equations (1), we employ the third-order-accurate Runge-Kutta (RK) Total Variation Diminishing (TVD) approach, introduced by Shu and Osher (1989). Denoting the time discretization operator by $\mathbb{S}[\mathbf{U}]$:

$$\left.\frac{\partial \mathbf{U}}{\partial t}\right|_{(i,j,k)} = \mathbb{S}\left[\mathbf{U}\right]\big|_{(i,j,k)} \equiv -\frac{\mathbb{F}_{(i+\frac{1}{2},j,k)} - \mathbb{F}_{(i-\frac{1}{2},j,k)}}{\Delta x} - \frac{\mathbb{G}_{(i,j+\frac{1}{2},k)} - \mathbb{G}_{(i,j-\frac{1}{2},k)}}{\Delta y} - \frac{\mathbb{H}_{(i,j,k+\frac{1}{2})} - \mathbb{H}_{(i,j,k-\frac{1}{2})}}{\Delta z} \quad (4)$$

the third-order RK-TVD scheme is given by

$$
\begin{aligned}
\mathbf{U}^{(1)}_{(i,j,k)} &= \mathbf{U}^{(n)}_{(i,j,k)} + \Delta t \cdot \mathbb{S}\left[\mathbf{U}^{(n)}\right]\Big|_{(i,j,k)} \\
\mathbf{U}^{(2)}_{(i,j,k)} &= \tfrac{3}{4}\mathbf{U}^{(n)}_{(i,j,k)} + \tfrac{1}{4}\left(\mathbf{U}^{(1)}_{(i,j,k)} + \Delta t \cdot \mathbb{S}\left[\mathbf{U}^{(1)}\right]\Big|_{(i,j,k)}\right) \\
\mathbf{U}^{(n+1)}_{(i,j,k)} &= \tfrac{1}{3}\mathbf{U}^{(n)}_{(i,j,k)} + \tfrac{2}{3}\left(\mathbf{U}^{(2)}_{(i,j,k)} + \Delta t \cdot \mathbb{S}\left[\mathbf{U}^{(2)}\right]\Big|_{(i,j,k)}\right)
\end{aligned}
\quad (5)
$$

where Δt is a time step, $^{(n)}$, $^{(1)}$, $^{(2)}$ and $^{(n+1)}$ denote the "old", "RK-intermediate" and "new" levels of time discretization, and $\mathbb{F}_{(i\pm\frac{1}{2},j,k)}$, $\mathbb{G}_{(i,j\pm\frac{1}{2},k)}$ and $\mathbb{H}_{(i,j,k\pm\frac{1}{2})}$ are numerical fluxes at the edges of the computational cell $_{(i,j,k)}$.

Space discretization. For discretization of numerical fluxes for each RK time discretization level $^{(m)}$, the third-order-accurate Godunov' conservative finite difference approach is utilized. In summary, we use the third-order-accurate MUSCL scheme (van Leer, 1979) for extrapolation of flow variables and characteristic fluxes from the cell centers to the cell edges, from the "left" and "right", e.g., $\mathbf{U}^{(m)}_{(i+r,j,k)}\big|_{r=-1,..,2} \leadsto \mathbf{U}^{(m),L/R}_{(i+\frac{1}{2},j,k)}$. The MUSCL scheme is supplemented by van Albada's limiter (van Albada et al., 1982). Then, the exact one-dimensional Riemann solver (Godunov et al., 1976) is applied to determine a new time level state of primitive variables $\mathbf{U}^{(m),L/R}_{\text{edge}} \leadsto \begin{bmatrix} P \\ \rho \\ V_\xi \end{bmatrix}^{(m+1)}_{\text{edge}}$, where V_ξ is a normal velocity for a particular edge. The tangential components of velocity $\left(V_\eta\right)^{(m+1)}_{\text{edge}}$ and $\left(V_\zeta\right)^{(m+1)}_{\text{edge}}$ for each edge are computed using a simple V_ξ-based upwinding procedure. Finally, the numerical fluxes at each edge $\mathbb{F}^{(m)}_{(i\pm\frac{1}{2},j,k)}$, $\mathbb{G}^{(m)}_{(i,j\pm\frac{1}{2},k)}$ and $\mathbb{H}^{(m)}_{(i,j,k\pm\frac{1}{2})}$ are computed using this Riemann-solver-based vector of primitive variables $\mathbf{V}^{(m+1)}_{\text{edge}} = \begin{bmatrix} P \\ \rho \\ V_\xi \\ V_\eta \\ V_\zeta \end{bmatrix}^{(m+1)}_{\text{edge}}$

3.2 The Level Set Method

For description of multimaterial interfaces, we will use the Level Set (LS) approach, introduced by Osher and Sethian in 1988. Within the Level Set approach, the evolution of the surface $\mathbb{I}$, moving in the direction normal to itself with a speed function $\mathbb{F}$, can be described by the following Hamilton-Jacobi equation:

$$\partial_t \varphi + \mathbb{F}\left|\nabla\varphi\right| = 0 \quad (6)$$

In the present work, the speed function $\mathbb{F}$ is defined as follows

$$\mathbb{F} \equiv w_j \cdot \partial_j \varphi \tag{7}$$

where w_j is a material velocity, which is equivalent to the following transport equation

$$\partial_t \varphi + \mathbf{w} \cdot \nabla \varphi = 0 \tag{8}$$

utilized by Mulder et al. (1992). This equation is numerically solved using the third-order RK-TVD scheme for time discretization and the fifth-order WENO$_5$ scheme for space discretization (Jiang and Peng, 2000). The level set is advanced in time at the beginning of each [(n)th] time step, decoupled from the RK-based time advancement of the gas dynamics equations (see section 3.1). To maintain the level set function as a signed distance function, a Partial Differential Equation-based (or "PDE-based") re-initialization procedure is applied, for which we use the WENO$_5$ scheme developed by Peng et al. (1999).

3.3 Boundary treatment: Characteristics-Based Matching (CBM)

The Characteristics-Based Matching (CBM) for one-sided (fluid-solid) interface has been originally introduced in (Nourgaliev et al., 2003) and further refined in (Nourgaliev et al., 2004a) and (Nourgaliev et al., 2004b). In the present section, we will describe its extension to two-sided (fluid-fluid) interfaces.

Types of nodes. After the level set function is updated at the beginning of each time step, the computational domain is separated into two regions, based on the sign of the level set function. The computational point $_{(i,j,k)}$ is declared to be occupied by fluid $_1$ if $\varphi_{(i,j,k)} > 0$ and by fluid $_2$ otherwise. Thus, for each fluid $_f$, one can define REAL zone (all nodes which are occupied by fluid$_f$) and GHOST zone (all nodes which are occupied by the other fluid), (Fedkiw et al., 1999). Next, based on the current value of the level set function, all computational nodes for each fluid are "tagged" into four different groups. For example, in the case of fluid $_1$:

    1. Real Boundary Nodes, RBNs. These are nodes which are located in the REAL region and in the close vicinity of the zero-level-set, i.e., $\varphi_{(i,j,k)} > 0$ and $\begin{bmatrix} \varphi_{(i\pm1,j,k)} \leq 0 & \text{or} \\ \varphi_{(i,j\pm1,k)} \leq 0 & \text{or} \\ \varphi_{(i,j,k\pm1)} \leq 0 \end{bmatrix}$.

    2. Real Nodes, RNs. These are all other nodes in the REAL region.

    3. Ghost Boundary Nodes, GBNs. These are nodes which are located in the GHOST region in the close vicinity of the zero-level-set, i.e., $\varphi_{(i,j,k)} \leq 0$ and $\begin{bmatrix} \varphi_{(i\pm1,j,k)} > 0 & \text{or} \\ \varphi_{(i,j\pm1,k)} > 0 & \text{or} \\ \varphi_{(i,j,k\pm1)} > 0 \end{bmatrix}$.

    4. Ghost Nodes, GNs. These are all other nodes in the GHOST region.

Computational nodes for fluid $_2$ are tagged similarly.

CBM points. As a next step, we identify all cross-sections of the zero-level-set with grid lines. These points are located between RBNs and GBNs, and they will be "tracked" along the gridlines and utilized as reference points for a 'Characteristics-Based Matching' of the numerical solution across the fluid-fluid interface. Each CBM point has two poles - Left and Right. We store $_{(i,j,k)}$ of the L-pole, the index $_{(f)}$ of the REAL fluid at the L-pole and the direction $_{(d)}$ of the gridline the CBM point belongs to. Possible directions are $_{(0)}, _{(1)}$ or $_{(2)}$ for x-, y- or z-directions, correspondingly. Also, the subcell position of the interface for each CBM point is computed from the level set function as

$$\theta_{\mathrm{CBM_p}} = \frac{|\varphi_{(i,j,k)}|}{|\varphi_{(i+1,j,k)}| + |\varphi_{(i,j,k)}|} \tag{9}$$

in the case of $_{(d=0),}$. Similar equations are applied for other directions. In addition, we sweep over all RBNs for each fluid and link them to correspondent CBM points.

Riemann solution. At the end of each RK-level of time advancement, the pseudo-multidimensional exact two-fluid Riemann solver is applied at each CBM point, using flow variables available at the L- and R-poles as the LEFT and RIGHT states, $\mathbf{U}_L$ and $\mathbf{U}_R$. Specifically, we apply the one-dimensional exact Riemann solver for two stiffened gases[1] (described in Godunov et al., 1976), to determine a new state of the interface, $\begin{bmatrix} P \\ \rho \\ V_\xi \end{bmatrix}^{(m+1)}_{CBM_p}$, where V_ξ is the normal component of velocity, corresponding to the direction $_{(d)}$ of the CBM point. For tangential components V_η and V_ζ, we make use of the fact that these components are Riemann invariants along normal direction (Cocchi and Saurel, 1997), and apply a simple upwinding procedure, described in section 3.2 of the paper by Cocchi and Saurel, 1997. Next, using the computed normal velocity, a new subcell position of the interface can be calculated as

$$\theta^{(m+1)}_{CBM_p} = \theta_{CBM_p} + V^{(m+1)}_\xi \frac{\Delta t}{\Delta h} \tag{10}$$

where Δh is a grid size in the direction $_{(d)}$. The new CBM states and "tracked" subcell position of the interface will be used when the numerical fluxes are computed at the beginning of the next RK step, and during the regularization procedure, described below.

Correction of fluxes. At each RK-stage, for each fluid, for each gridline direction, after the numerical fluxes are computed as described in section 3.1, we identify all computational nodes which are in the vicinity of CBM points within the stencil range of the numerical scheme for spatial discretization. The numerical fluxes for these points are recomputed. Before that, we scan the neighborhood of these nodes and fill all GBNs and GNs, which are within the stencil range, by flow variable values taken from the relevant CBM points.

Regularization procedure. At the end of each RK-level, after all RNs and RBNs for each fluid are updated, it is necessary to correct solution at all RBNs in order to eliminate numerical errors due to numerical diffusion and the use of the single-fluid-based Riemann solver at these points. The most straightforward regularization strategy is to use an interpolation between the solution in RNs and CBM points. In *one-dimension*, we apply the following interpolation procedure.

Sweep over all RBNs of each fluid. From the linked CBM point, we know the direction in which the interface is located (left or right), and the CBM solution at the interface. Suppose the interface is located to the left of the RBN node $_{(i)}$. In this case, the value of flow variable Ψ_{RBN} is corrected as:

$$\Psi^{(m+1)}_{(i)} = \begin{cases} \Psi^{(m+1)}_{CBM_p} & \text{if} \quad \theta^{(m+1)}_{CBM_p} < 0 \\ \Psi^{(m+1)}_{(i-1)} - \frac{\Psi^{(m+1)}_{(i-1)} - \Psi^{(m+1)}_{CBM_p}}{1 + \theta^{(m+1)}_{CBM_p}} & \text{otherwise} \end{cases} \tag{11}$$

If the interface is located to the right of the RBN node, the following interpolation formula is applied:

$$\Psi^{(m+1)}_{(i)} = \begin{cases} \Psi^{(m+1)}_{CBM_p} & \text{if} \quad \theta^{(m+1)}_{CBM_p} > 1 \\ \Psi^{(m+1)}_{(i+1)} - \frac{\Psi^{(m+1)}_{(i+1)} - \Psi^{(m+1)}_{CBM_p}}{2 - \theta^{(m+1)}_{CBM_p}} & \text{otherwise} \end{cases} \tag{12}$$

---

[1]In the case of another equation of state, the exact Riemann solver can be constructed as described by Menikoff and Plohr, 1989.

We define two CBM regularization techniques. The first one will be called "Full-fix" (CBM_{F-fix}). In this regularization the whole vector of primitive variables $\mathbf{V}$ is corrected. In this case, our regularization is very similar to the one used by Cocchi and Saurel (1996). The second regularization technique will be called "Entropy-fix" (CBM_{E-fix}). In this case, only entropy will be interpolated, $\Psi = S$. This interpolated entropy is used to correct density of the RBN. Pressure and velocity stay untouched. This regularization is similar to the constant-entropy-isobaric-fix, used in the Ghost Fluid Method (Fedkiw et al., 1999). The CBM_{E-fix} is less intrusive and, therefore, preferable.

Multidimensions. Extension of the above described regularization techniques to multiple dimensions is realized using the following simple iterative procedure for each fluid.

$\Rightarrow$ p=1. Start iterative loop:

1. p++. $\mathcal{E} = 0$.
2. Run over all RBNs and store the current iteration value of $\Psi_{RBN}^{(p)}$.
3. Run over all RBNs. For each RBN apply the following weighted dimension-by-dimension interpolation procedure.

   (a) Loop over all directions. For each direction, check if any CBM point exist to the left and to the right. There are four options:

   i. *There are no interfaces to the left and to the right.* Suppose $(d=0)$. In this case, the correction $\tilde{\Psi}_{(0)}$ is

   $$\tilde{\Psi}_{(0)} = \frac{\Psi_{(i+1,j,k)}^{(m+1)} + \Psi_{(i-1,j,k)}^{(m+1)}}{2}$$

   Similar formulas can be applied for $\tilde{\Psi}_{(1)}$ and $\tilde{\Psi}_{(2)}$.

   ii. *The interface is located to the left of the RBN.* In this case, the correction $\tilde{\Psi}_{(d)}$ is computed as described by eq.(11).

   iii. *The interface is located to the right of the RBN.* In this case, the correction $\tilde{\Psi}_{(d)}$ is computed as described by eq.(12).

   iv. *There are two interfaces, to the left and to the right of the RBN.* In this case, a simple algebraic averaging between $\Psi_{CBM_p}^{(m+1),L}$ and $\Psi_{CBM_p}^{(m+1),R}$ is used.

   (b) Update Ψ at the RBN as:

   $$\Psi_{RBN}^{(p+1)} = \sum_{(d)} \xi_d^2 \tilde{\Psi}_{(d)}$$

   where ξ_d are components of the normal vector, computed at the RBN using the level set function, $\vec{\xi} = \frac{\nabla \phi}{|\nabla \phi|}$.

4. Run over all RBNs. For each RBN, update Ψ as $\Psi_{(i,j,k)}^{(m+1)} = \Psi_{RBN}^{(p+1)}$ and increment $\mathcal{L}_1$-norm of the error as $\mathcal{E} +=|\Psi_{RBN}^{(p+1)} - \Psi_{RBN}^{(p)}|$.
5. Check for a convergence. If $\frac{\mathcal{E}}{N} < \epsilon$ (where N and ϵ are the total number of RBNs and the tolerance level, respectively), finish the iteration loop. Otherwise - keep going.

$\Leftarrow$ Finish iterative loop.

The above described iterative procedure converges in 5-10 iterations.

Population of GBNs. Even though the GBNs will not actively participate in the numerical flux calculation at the next time step, these nodes must be populated, because some of them are to be converted into RBNs due to the motion of the interface. Thus, after all RBNs are corrected as described above, all GBNs are re-populated using the first-order-accurate PDE-based extrapolation technique (Peng et al., 1999).

Velocity for transport of LS. Finally, we note that the Riemann solutions for velocity at the CBM points can be used to correct velocities utilized for time advancement of the level set equation (8). First, the vector field $\mathbf{w}$ is set to be equal to the material velocity $\mathbf{u}$. Second, for each CBM point, we correct $\mathbf{w}$ at both poles using the value of the material velocity computed at the CBM point. Finally, we apply a PDE-based extrapolation technique to form an "extension velocity" field (Sethian, 1999), $\mathbf{w}$, which will be used to advance the level set. This procedure is known to help to suppress mass conservation errors and to maintain the level set as a signed distance function (Sethian, 1999).

4 Numerical Examples

In this section, the CBM approach introduced above will be examined on a number of multiphase gas/liquid and gas/solid problems. First, the approach is applied for simulation of two one-dimensional gas/liquid and gas/solid shock-tube problems, in order to test the accuracy and robustness of the method, section 4.1. Second, in section 4.2, we will consider a two-dimensional gas/liquid problem (shock-induced collapse of a cylindrical air cavity in water), for which the reference numerical solution exists in the literature. The computational results with our Eulerian approach are compared to those of the Free-Lagrange method (Ball et al., 2000). Finally, the CBM approach is applied to study shock wave interaction with a liquid drop, in section 4.3.
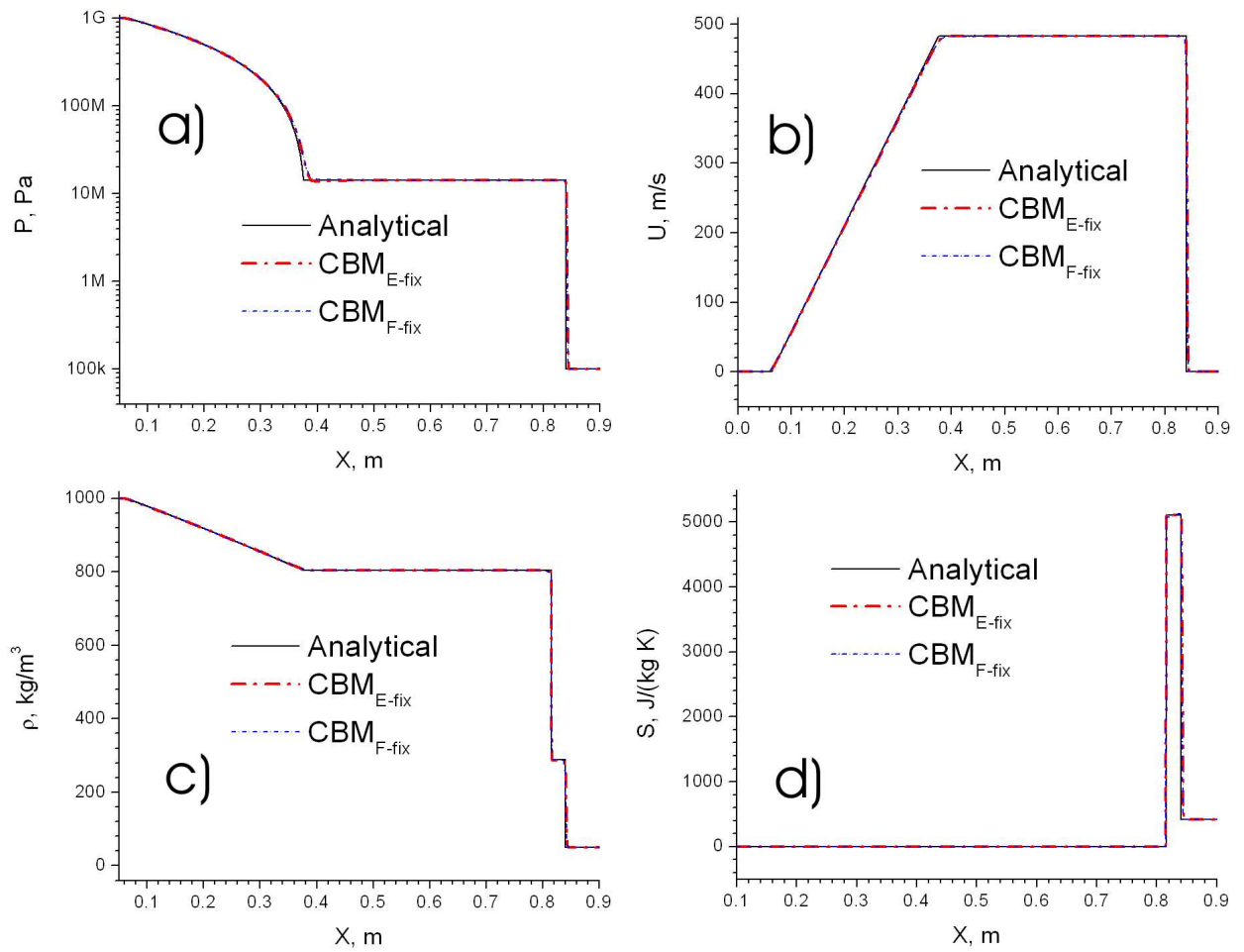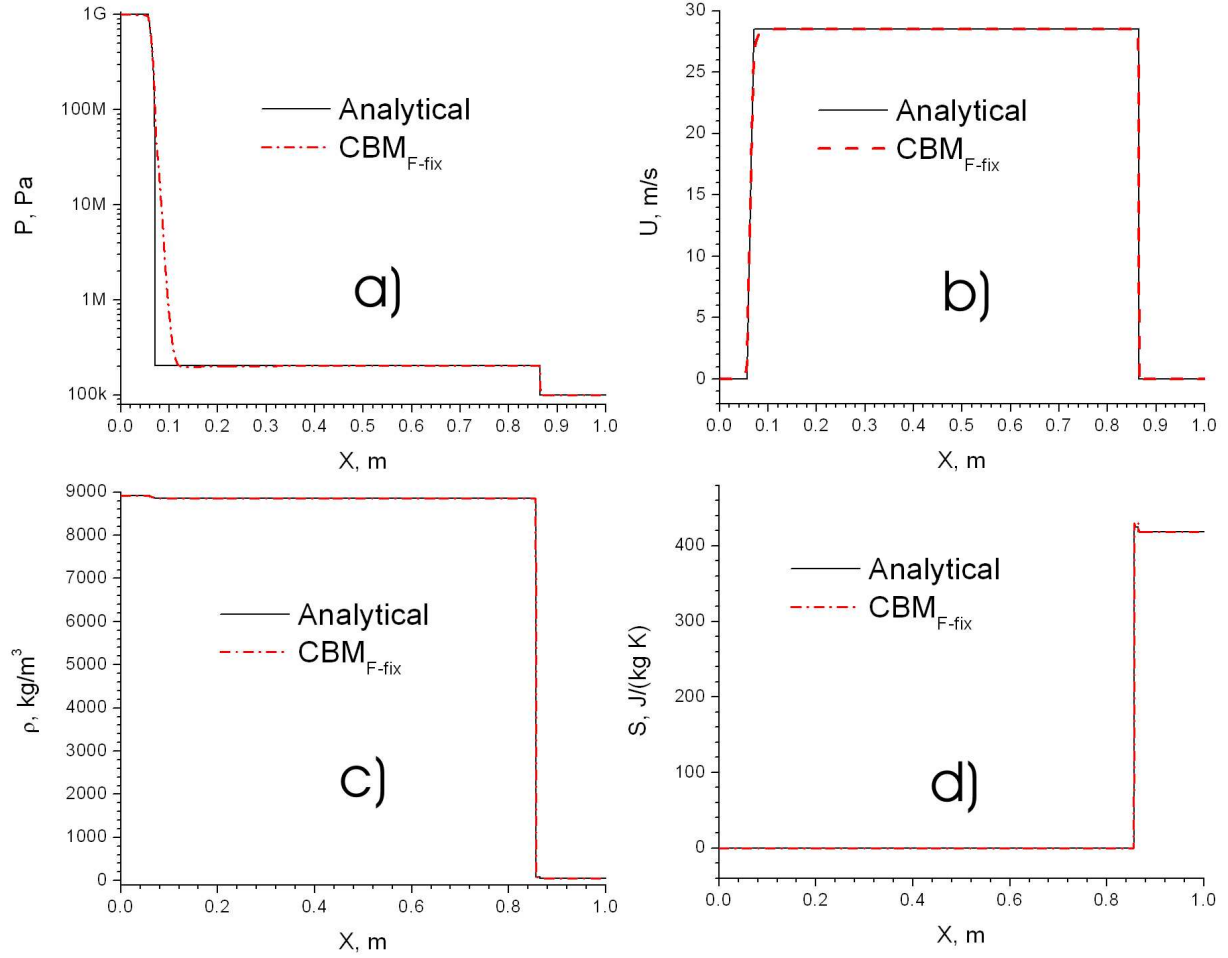

Figure 1: *Water-air shock-tube problem.*

Figure 2: *Copper-air shock-tube problem.*

4.1   Examples I and II: One-Dimensional Shock Tube Problems

Example I. As our first numerical example, we will consider a gas-liquid shock-tube test, introduced by Saurel and Abgrall (1999). The conditions of this test correspond to a severe air-water shock tube, with interface located at $x = 0.7$ m, with initial "Left" and "Right" states specified as

$$
\begin{aligned}
\left(\rho, u, p, \gamma, \Pi\right)_{\mathrm{L}} &= \left(1000,\, 0,\, 10^9,\, 4.4,\, 6 \cdot 10^8\right) \\
\left(\rho, u, p, \gamma, \Pi\right)_{\mathrm{R}} &= \left(50,\, 0,\, 10^5,\, 1.4,\, 0\right)
\end{aligned}
\tag{13}
$$

Simulations are performed using a computational grid with $\Delta x = \frac{1}{800}$ m and CFL number of 0.85. Both the $\mathrm{CBM}_{\mathrm{F\text{-}fix}}$ and $\mathrm{CBM}_{\mathrm{E\text{-}fix}}$ techniques are tested. For the level set, no re-initialization procedure is used. The analytical and computed profiles of pressure, velocity, density and entropy for $t = 240$ μsec are plotted in Fig.1. As it can be seen, our approach produced excellent results, for both "Full-fix" and "Entropy-fix" versions of the method. Importantly, in difference to the model by Saurel and Abgrall (1999), there are no density oscillations near gas-liquid interface and overshoots of velocity at the rarefaction wave, see Fig.3 of the paper (Saurel and Abgrall, 1999). Also, we found that the "Constant-Entropy-Isobaric-Fix Ghost Fluid Method" (GFM), developed by Fedkiw et al. (1999), performs poorly for this problem. In order to make the GFM stable, the CFL number must be reduced to 0.15. With our CBM interface treatment, the scheme is stable for CFL≤ 1.

Example II. In our next numerical test, we will push the limits of the method by considering gas-solid interface. The previous test is modified substituting water by copper (parameters for a stiffened gas EOS are taken from Saurel and Abgrall, 1999), with initial discontinuity located at $x = 0.85$ m:

$$
\begin{aligned}
(\rho, u, p, \gamma, \Pi)_{\mathrm{L}} &= (8924,\ 0,\ 10^9,\ 4,\ 3.41 \cdot 10^{10}) \\
(\rho, u, p, \gamma, \Pi)_{\mathrm{R}} &= (50,\ 0,\ 10^5,\ 1.4,\ 0)
\end{aligned}
\tag{14}
$$

The numerical solution is obtained using the $\mathrm{CBM}_{\mathrm{F\text{-}fix}}$ approach on computational grid of $\Delta x = \frac{1}{3200}$ m and CFL number 0.8. As shown in Fig.2, there is an excellent agreement between the CBM method and analytical solution, both plotted for $t = 200$ μsec. It is instructive to note that the original GFM method (Fedkiw et al., 1999) is unstable for this numerical test, even under extremely low CFL number conditions.

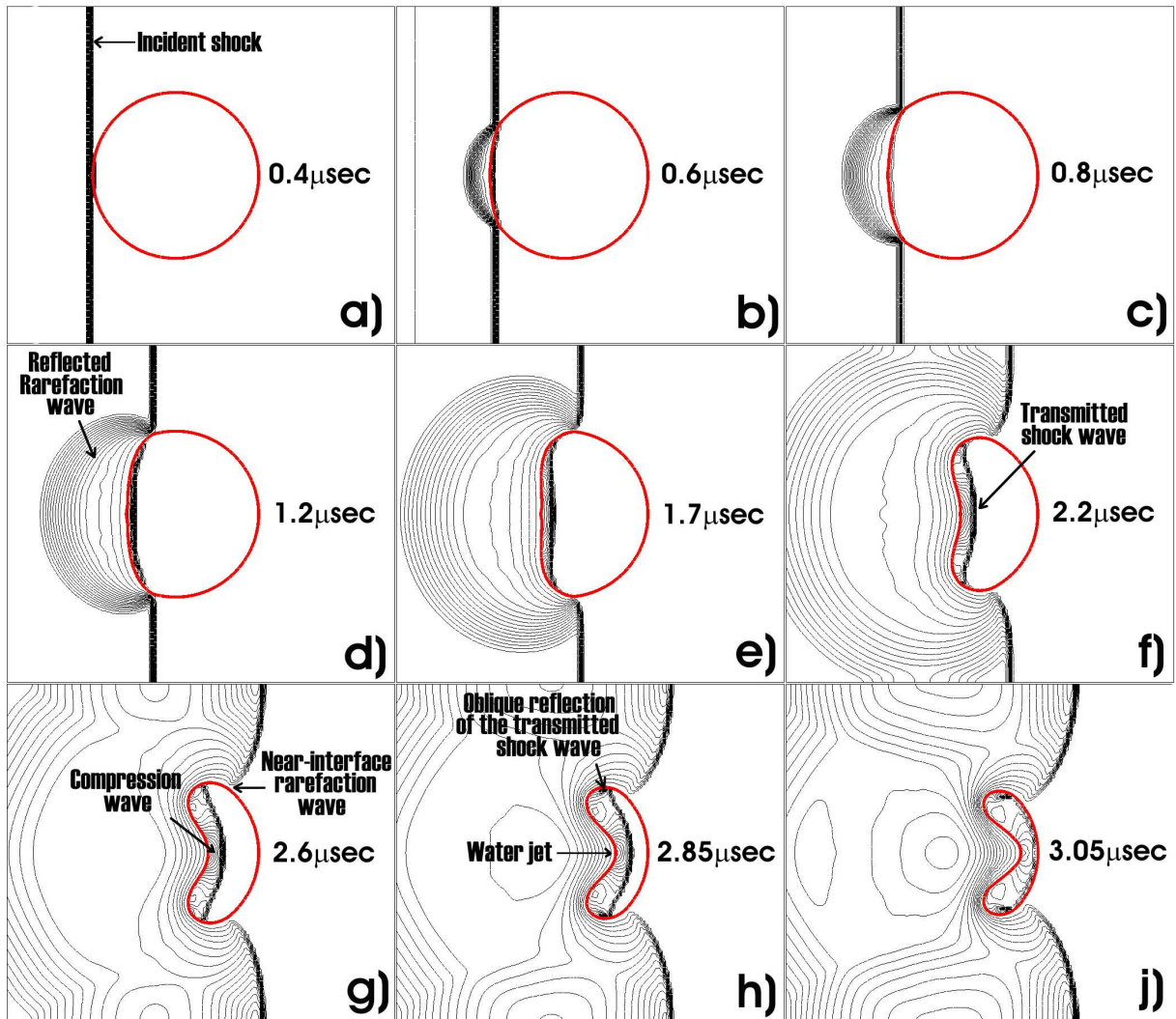## 4.2 Example III: Shock-Induced Collapse of a Cylindrical Air Cavity in Water

Figure 3: *Dynamics of pressure field and shape of bubble for shock/cavity interaction test. Grid resolution is 100 nodes per diameter of bubble.*

As our first two-dimensional example, we will consider a collapse of a cylindrical air cavity in water. This problem was studied previously by Ball et al. (2000), using a Free-Lagrange simulation
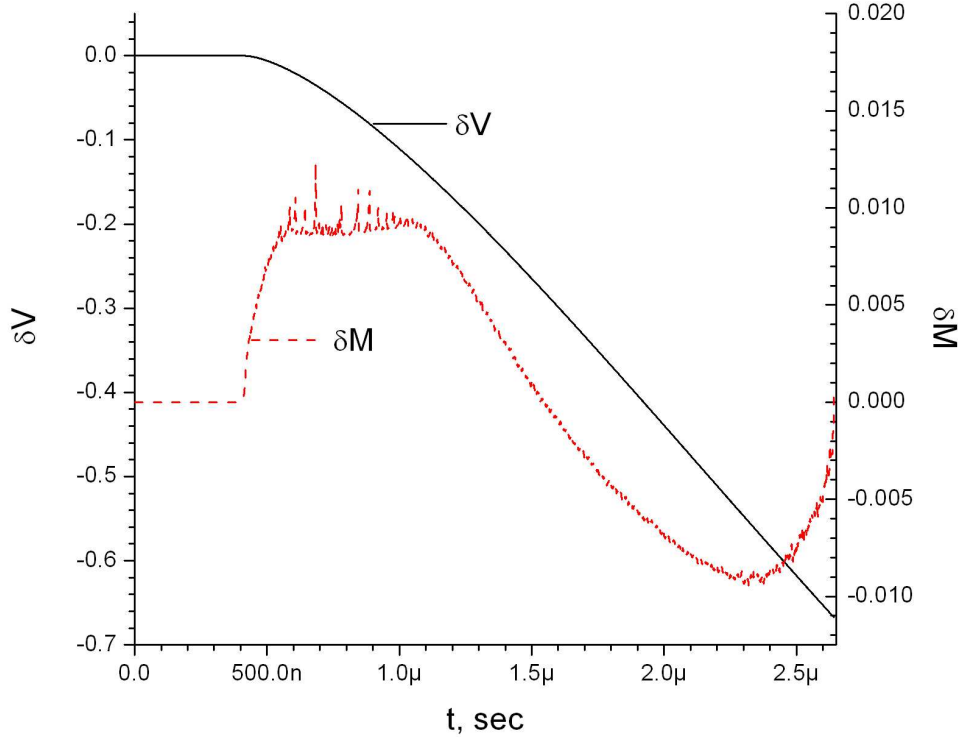
Figure 4: *Dynamics of cavity's volume and conservation of mass for shock-induced collapse of a cylindrical air cavity in water. Grid resolution is 200 nodes per diameter of bubble.*

approach.

Problem formulation. A cylindrical air bubble, 6 mm in diameter, is immersed in a water pool, under the following initial conditions: $u = 0$ m/s, $P = 10^5$ Pa, $\rho_{\text{air}} = 1$kg/m^3 and $\rho_{\text{water}} = 1000$ kg/m^3. The center of the bubble is located at the position $\mathbf{r}_{\text{b}} = (6, 6)$ mm in the computational domain of size 13.8×12 mm. The liquid and gas are modeled using a stiffened equation of state with parameters $\begin{bmatrix} \gamma = & 4.4 \\ \Pi = & 6 \cdot 10^8 \end{bmatrix}$ and $\begin{bmatrix} \gamma = & 1.4 \\ \Pi = & 0 \end{bmatrix}$ for water and air, correspondingly. A planar incident M_{sh}=1.715 shock wave is initially located 4.2 mm to the left of the air bubble's center. The post-shock conditions are: $\mathbf{V}_{\text{post-shock}} = \begin{bmatrix} P & = & 1.9\,\text{GPa} \\ \rho & = & 1323.6478\,\text{kg/m}^3 \\ u & = & 681.577871\,\text{m/s} \\ v & = & 0\,\text{m/s} \end{bmatrix}$. Simulations are performed using two computational grids: 230×200 and 460×400, which corresponds to a resolution of 100 and 200 computational nodes per initial bubble diameter. At the top and bottom boundaries of the domain, we applied periodical boundary conditions. Non-reflection boundary conditions are utilized at the left and right boundaries of the domain. In this example, the "Full-fix" CBM$_{\text{F-fix}}$ coupling strategy is employed. The LS re-initialization procedure is applied every 25 time steps.

Flow dynamics. The results of the computations are shown in Figs.3 and 4. The dynamics of flow evolution modeled by our Eulerian approach is very similar to the one described by Ball et al. (2000), who employed a Lagrangian method. Due to the large acoustic impedance of water, the incident water shock transmits a relatively weak shock into the air, producing a strong reflected rarefaction wave in the water, see Figs.3d,f. The pressure fields in water and air are plotted with 20 uniformly distributed isolines. To contrast the transmitted shock in air, the maximum/minimum ranges of isolines were

set independently for water and air. It is instructive to note that the transmitted shock is only *relatively* weak. In fact, the post-shock pressure is quite high $P_{\text{post-shock}}$=2.3 MPa, which corresponds to $M_{\text{shock}} = 4.7$. Due to higher water velocity at the centerline, there is an additional compression wave generated in the air, which tends to strengthen the transmitted air shock, Fig.3g. After the incident shock passed the equator of the air bubble at approximately $t = 1.7$ μsec, the interaction of the incident shock with rarefaction waves, generated near gas-liquid interface (Fig.3g), resulted in significant weakening and curvature of the incident shock. At the same time, the transmitted air shock travels more slowly. By approximately 2 μsec, the air bubble becomes involuted, with distinct water jet formed at the centerline, Figs.3f-h. Starting from approximately 2.85 μsec, the transmitted air shock forms an oblique reflection, marked in Fig.3h.

Volume ratio. Time history of the air cavity volume ratio $\delta V \equiv \frac{V_c(t)}{V_c(t=0)}$ is shown in Fig.4. The volume of the cavity V_c for time moment t is computed using a piecewise-linear reconstruction of the interface based on cross-sections of zero-level-set with gridlines. Starting from approximately 1 μsec, the cavity' volume reduces almost linearly, which is consistent with the results presented by Ball et al. (2000).

Mass conservation. Finally, we show the history of mass conservation errors in Fig.4. Even though our approach is formally non-conservative near interface due to both the level set formulation and non-conservative boundary treatment, the actual loss of mass, defined as $\delta M \equiv \frac{M_c(t)}{M_c(t=0)}$, is remarkably low and below 1% for grid resolution of 200 nodes per bubble' diameter. The instantaneous mass of the air cavity is computed by summation of mass over all REAL gas cells, $M_c = \sum_{\text{REAL}} \Delta M_{i,j,k}$, $\Delta M_{i,j,k} = \rho_{i,j,k} \Delta V_{i,j,k}$, where the local volumes of RBNs $\Delta V_{i,j,k}^{\text{RBN}}$ are computed using the piecewise-linear reconstruction discussed above.

4.3   Example IV: Interaction of a Planar Shock with a Water Column

In our final numerical example, we will consider interaction of a planar shock wave with a cylindrical water column.

Problem formulation. A cylindrical water column is generated at the center of the computational domain of size 20.8×20.8 mm. The diameter of the column is 6.4 mm. Initially, the water column is suspended in motionless air, under the following conditions $u = 0$ m/s, $P = 0.1$ MPa, $\rho_{\text{air}} = 1$ kg/m^3 and $\rho_{\text{water}} = 1000$ kg/m^3. The following parameters of the stiffened equation of state are used $\begin{bmatrix} \gamma = & 7.415 \\ \Pi = & 2.963 \cdot 10^8 \end{bmatrix}$ and $\begin{bmatrix} \gamma = & 1.4 \\ \Pi = & 0 \end{bmatrix}$ for water and air, correspondingly. A planar incident M_{sh}=1.47 shock wave is traveling from the left of the water column. Correspondent post-shock air flow conditions are: $\mathbf{V}_{\text{post-shock}} = \begin{bmatrix} P & = & 0.23544\,\text{MPa} \\ \rho & = & 1.8106\,\text{kg/m}^3 \\ u & = & 246.241\,\text{m/s} \\ v & = & 0\,\text{m/s} \end{bmatrix}$. Initial position of the incident shock is 11.2 mm to the left of the water column's center. Boundary conditions are periodical in vertical direction and non-reflection for both left and right boundaries of the domain. The simulation is performed using the $\text{CBM}_{\text{E-fix}}$ coupling strategy, with grid resolution of 160 computational nodes per column's diameter.
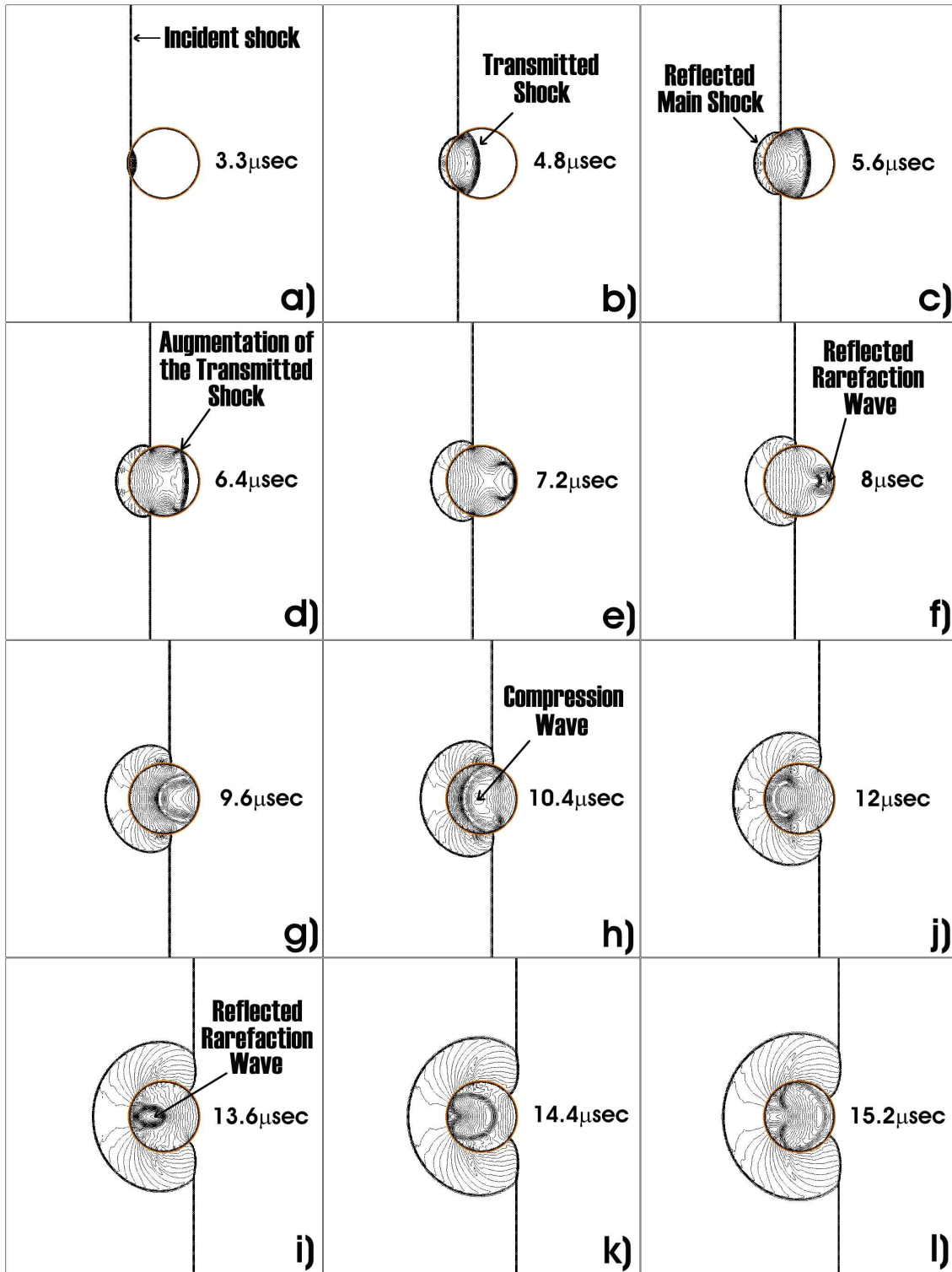
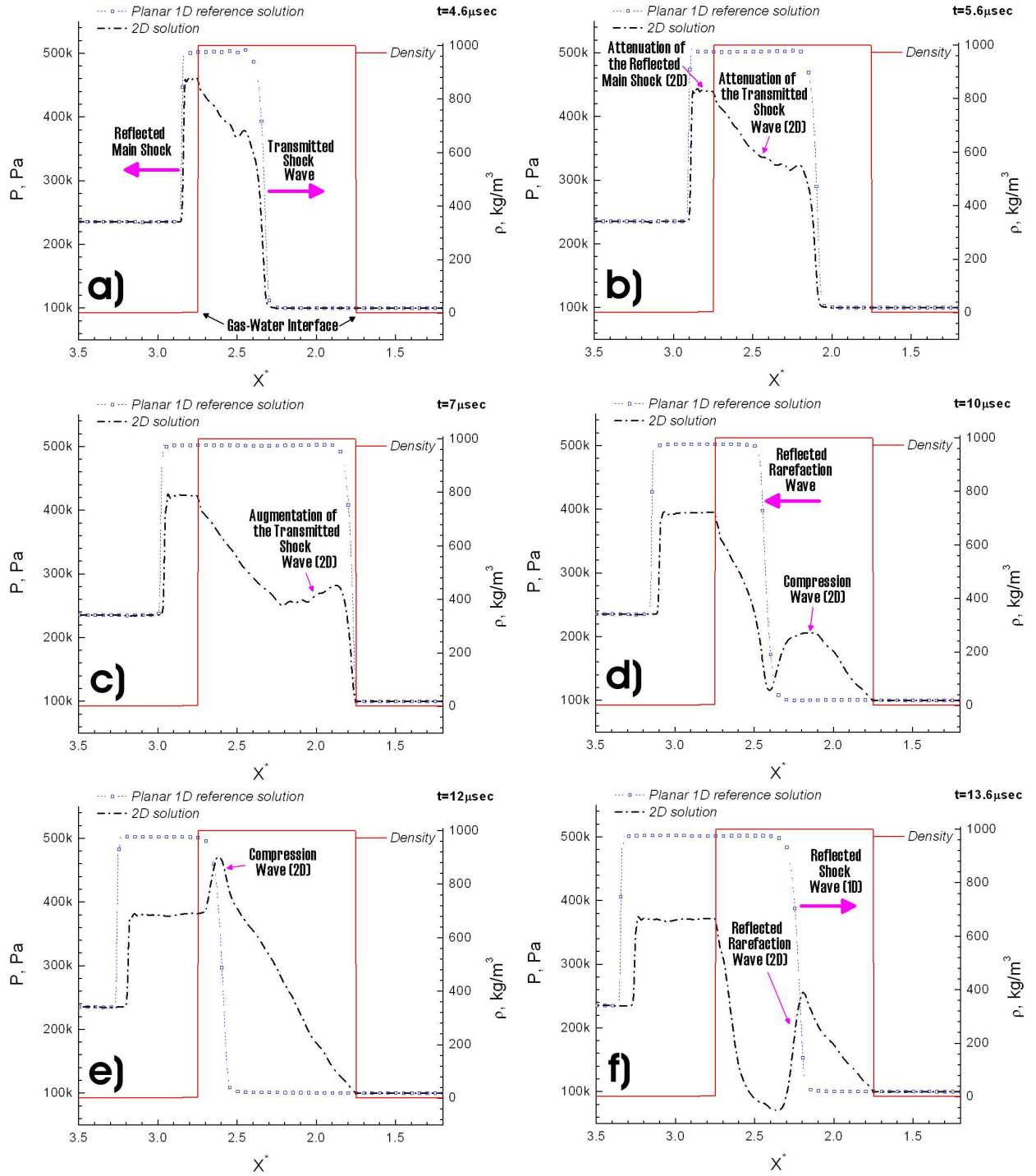Figure 5: *Interaction of a planar shock with a water column: dynamics of the pressure field.*

Figure 6: *Interaction of a planar shock with a water column: distribution of pressure along centerline as a function of time.*

"Reference" 1D solution. It is instructive to consider first a correspondent one-dimensional problem, in which the incident shock interacts with a layer of water of equivalent thickness. The analytical solution for the first impact of the shock upon the left boundary of the fluid layer is

$$
\Leftarrow \textbf{Reflected M}_{\text{sh}}\textbf{=0.827 shock} \quad \Big| \quad \textbf{Transmitted M}_{\text{sh}} = \textbf{1.0004 shock} \Rightarrow
$$

$$
\Leftarrow \mathbf{V}_{\text{Post-shock}} = \begin{bmatrix} P = 5.02\,\text{bar} \\ \rho = 3.072\,\text{kg/m}^3 \\ u = 0.27\,\text{m/s} \end{bmatrix} \quad \Big| \quad \mathbf{V}_{\text{Post-shock}} = \begin{bmatrix} P = 5.02\,\text{bar} \\ \rho = 1000.183\,\text{kg/m}^3 \\ u = 0.27\,\text{m/s} \end{bmatrix} \Rightarrow \quad \Big| \qquad (15)
$$

$$
\text{Air} \qquad\qquad \text{Water} \qquad\qquad \text{Air}
$$

Next, the transmitted shock hits the right boundary of the fluid layer, which produces the reflected rarefaction wave and extremely weak transmitted shock:

$$
\Longleftarrow \textbf{Reflected Rarefaction wave} \quad \Big| \quad \textbf{Transmitted M}_{\text{sh}} = \textbf{1.0009 shock} \Longrightarrow
$$

$$
\Leftarrow \mathbf{V}_{\text{Post-wave}} = \begin{bmatrix} P = 1.002\,\text{bar} \\ \rho = 1000.0001\,\text{kg/m}^3 \\ u = 0.5423\,\text{m/s} \end{bmatrix} \quad \Big| \quad \mathbf{V}_{\text{Post-shock}} = \begin{bmatrix} P = 1.002\,\text{bar} \\ \rho = 1.0015\,\text{kg/m}^3 \\ u = 0.5423\,\text{m/s} \end{bmatrix} \Rightarrow \qquad (16)
$$

$$
\text{Air} \qquad\qquad \text{Water} \qquad\qquad \text{Air}
$$

The rarefaction wave travels back to the left boundary of the fluid layer and reflects from it as a shock. Thus, the shock wave in water layer is "trapped" between two interfaces, oscillating with a period of approximately 8.6 μsec.

Dynamics of flow in 2D. In the case of a cylindrical water column, due to the divergent geometry of the interface, the transmitted shock in water weakens during the first 3 μsec of its journey across the water column - up to the moment when it reaches the equator, see Figs.5c and 6b. Then, the convergent geometry of the interface at the right half of the drop strengthen the transmitted shock, as seen from Figs.5d and 6c. Note, that the speed of the transmitted shock is consistent with the 1D reference solution, also shown in Fig.6. Next, the transmitted shock is reflected from the left side of the water column as a rarefaction wave, Fig.5f. By that time, the two dimensional solution is already significantly deviated from the one-dimensional one. The reflected rarefaction wave is about to travel back across the liquid, which is colder than in the case of fluid layer. Furthermore, in difference to the 1D case, there is a compression wave, which is generated as a consequence of the focussing geometry of the interface in the right half of the water column, see Figs.5h and 6d. This compression wave follows the rarefaction wave with higher speed - and it eventually takes over, as it can be seen in Fig.6e. The whole forward and back cycle takes approximately the same time as in the case of fluid layer, i.e. 8.6 μsec. However, the start of the second cycle is completely different. In difference to the formation of the *reflected shock wave* (1D case), the second cycle of the 2D case starts with the *reflected rarefaction wave*. The oscillation of 2D case decays quickly in another couple of forward and back cycles.

Finally, the comparison of our numerical solution with the experimental holographic interferogram for gas flow around a water droplet is shown in Fig.7. The idealized numerical Schlieren image presented in Fig.7b is generated in the exact same manner as described in section 3.3 of (Quirk and Karni, 1996), using the attenuation coefficient $\kappa = 40$. As it can be seen, there is an excellent agreement of the computed flow field with the experimental image.
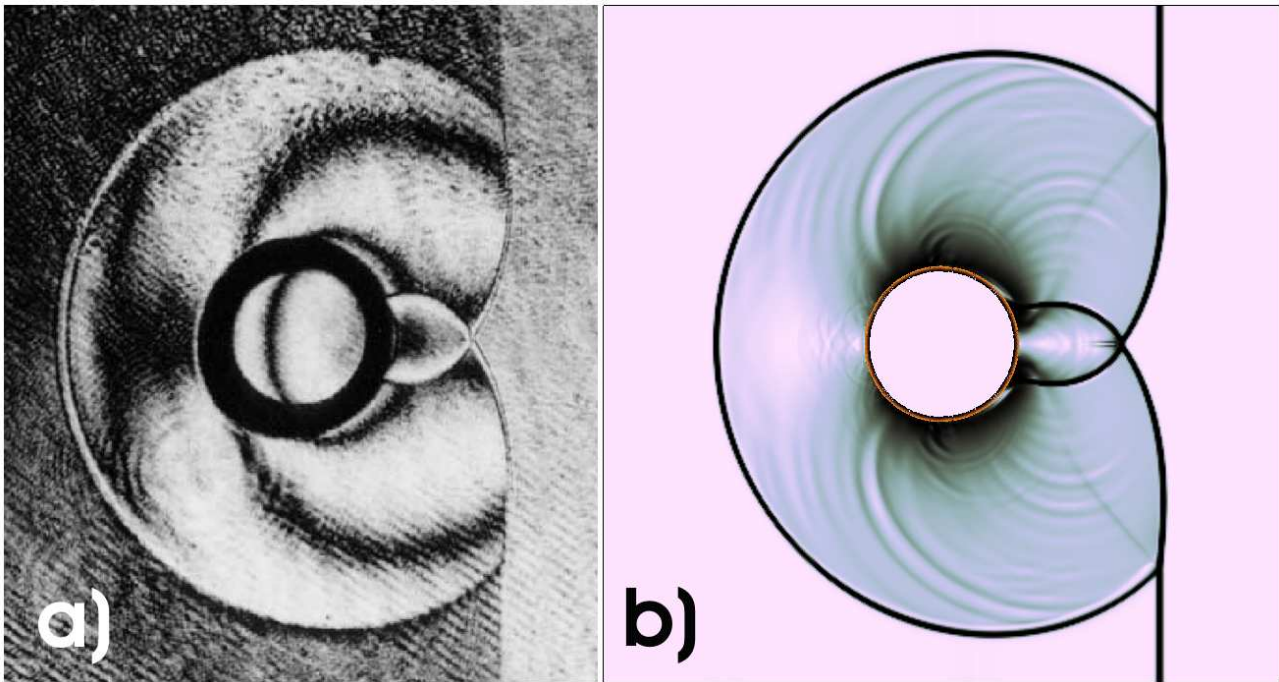
Figure 7: *a) Experimental infinite fringe double exposure holographic interferogram (Igra and Takayama, 2001), t=23μsec. b) Idealized numerical Schlieren (present study).*

5 Conclusion

This paper is concerned with an emergent class of compressible, high-speed, multi-material flow, problems. Specifically, we are interested in computational simulation capabilities to accurately describe and effectively analyze interactions, deformation and breakup of dispersed solid and fluid entities (bubbles, drops) in high-speed flows, e.g. under explosion and shock wave conditions. The physics of such intense interactions is complex, and their extreme conditions (velocity, pressure) limit the extent by which available diagnostic methods can be useful in quantifying the interaction details. In such a situation, the methods of direct numerical simulation (DNS), and increasingly accessible computing power, have been seen as a complementary, or even perhaps the central avenue towards a basic understanding. However, compared to other fields of fluid dynamics, the use of the DNS as an investigation method for compressible multiphase flows has hardly began.

In this paper, we contribute to this early development of the subject by a novel approach for the treatment of high-impedance, gas-liquid and gas-solid interfaces. Our basic guidance in this development is to respect the information flow in inherently transient and complex flow and pressure fields across multi-material domains. We achieve this objective through a consistent use of numerical schemes based on Riemann problem solutions in both single-fluid interior domains and two-fluid interfacial regions. We bring to bear best features of front-tracking and front-capturing techniques, namely the accuracy of the interface boundary condition treatment in the former and the algorithmic simplicity for the interface geometry treatment in the later.

The resulting method, named the 'Characteristics-Based Matching' (CBM), is Eulerian-grid-based, and uses a level-set technique to capture the multi-dimensional complex topology of evolving interfaces, including breakup and coalescence. To compute flow variables at the Eulerian nodes,

we employ the third-order accurate Runge-Kutta Total Variation Diminishing approach for time discretization. For space discretization, we use the third-order-accurate Godunov's (single-fluid-Riemann-solution-based) conservative finite-difference scheme. Most importantly, to determine the interface's state variables (pressure, density and velocity), we utilize the pseudo-multidimensional implementation of the exact two-fluid Riemann solution. The key idea in such a treatment is to accurately account for complex interactions of shock and rarefaction waves with multimaterial interfaces. We found this step essential for control of unphysical numerical instabilities (pressure oscillations, overheating) when materials on different sides of the interface feature significantly different properties (e.g., density, stiffness). We use the exact-Riemann-solution-based velocity to advance the interface along the gridlines, in a manner similar to the front tracking techniques. The solutions in these "tracked" interface points (based on the two-fluid Riemann solver) and the Eulerian-based interior domain (based on the single-fluid Riemann solver) are coupled by an interpolation scheme, which also helps to regularize the numerical solution near the interface.

In the paper, we show that the CBM method is capable of providing accurate solutions for a number of challenging test problems of shocks interacting with a compressible solid (copper), gas bubble, and a stiff fluid (water).

References

[1] Abgrall, R., 1988, Generalization of Roe Scheme for the Computation of Mixture of Perfect Gases, *Rech. Aérosp.*, **6**, p.31.

[2] Abgrall, R., 1996, How to Prevent Pressure Oscillation in Multicomponent Flow Calculation: a Quasi-Conservative Approach, *Journal of Computational Physics*, **125**, pp.150-160.

[3] Abgrall, R., and Karni, S., 2001, Computations of Compressible Multifluids, *Journal of Computational Physics*, **169**, pp.594-623.

[4] Ball, G.J., Howell, B.P., Leighton, T.G., and Schofield, M.J., 2000, Shock-Induced Collapse of a Cylindrical Air Cavity in Water: a Free-Lagrange Simulation, *Shock Waves*, **10**, pp.265-276.

[5] Benson, D.J., 1992, Computational Methods in Lagrangian and Eulerian Hydrocodes, *Comput. Methods Appl. Mech. Engrg.*, **99**, pp.235-394.

[6] Cocchi, J.-P., and Saurel, R., 1997, A Riemann Problem Based Method for the Resolution of Compressible Multimaterial Flows, *Journal of Computational Physics*, **137**, pp.265-298.

[7] Chern, I.L., Glimm, J., McBryan, O., Plohr, B., and Yaniv, S., 1985, Front Tracking for Gas Dynamics, *Journal of Computational Physics*, **62**, pp.83-110.

[8] Fedkiw, R.P., Aslam, T., Merriman, B., and Osher, S., 1999, A Non-oscillatory Eulerian Approach to Interfaces in Multimaterial Flows (the Ghost Fluid Method), *Journal of Computational Physics*, **152**, pp.457-492.

[9] Godunov, S.K., Zabrodin, A.V., Ivanov, M.Ya., Kraiko, A.,N., and Prokopov, G.P., 1976, Numerical Modeling of Multdimensional Gas Dynamics Problems, (In Russian), *Nauka*, Moscow, 1976.

[10] Glimm, J., Grove, J.W., Li, X.L., Shyue, K.-M., Zeng, Y., and Zhang, Q., 1998, Three-Dimensional Front Tracking, *SIAM Journal on Scientific Computing*, **19**, pp.703-727.

[11] Jiang, G.S., and Peng, D.P., 2000, Weighted ENO schemes for Hamilton-Jacobi equations, *SIAM Journal on Scientific Computing*, **21**(6), pp.2126-2143.

[12] Igra, D., and Takayama, K., 2001, Numerical Simulation of Shock Wave Interaction with a Water Column, *Shock Waves*, **11**, pp.219-228.

[13] Karni, S., 1996, Hybrid Multifluid Algorithms, *SIAM Journal on Scientific Computing*, **17**(5), pp.1019-1039.

[14] Mair, H. U., 1999, Review: Hydrocodes for Structural Response to Underwater Explosion, *Shock and Vibration*, **6**(2), pp.81-96.

[15] Menikoff, R., and Plohr, B.J., 1989, The Riemann Problem for Fluid Flow of Real Materials, *Reviews of Modern Physics*, **61**(1), pp.75-130.

[16] Mulder, W., Osher, S., and Sethian, J.A., 1992, Computing Interface Motion in Compressible Gas Dynamics, *Journal of Computational Physics*, **100**, pp.209-228.

[17] Nourgaliev, R.R., Dinh, T.N., Suschikh, S.Yu., Yuen, W.W., and Theofanous, T.G., 2003, The Characteristics-Based Matching Method for Compressible Flow in Complex Geometries, *AIAA 2003-0247*, *41st AIAA Aerospace Sciences Meeting and Exhibit*, January 6-9, 2003, Reno, NV, USA.

[18] Nourgaliev, R.R., Dinh, T.N., and Theofanous, T.G., 2004a, The Level-Set-Based Cartesian Grid Method for High-Speed Multiphase Fluid-Solid (Particulate) Flows, *CRSS Research Report 01/04-1*, 50p., January 1, 2004.

[19] Nourgaliev, R.R., Dinh, T.N., and Theofanous, T.G., 2004b, The 'Characteristics-Based Matching' (CBM) Method for Compressible Flow with Moving Boundaries and Interfaces, *ASME Journal of Fluids Engineering* (in press).

[20] Quirk, J.J., and Karni, S., 1996, On the Dynamics of a Shock-Bubble Interaction, *Journal of Fluid Mechanics*, **318**, pp.129-163.

[21] Peng, D.P., Merriman, B., Osher, S., Zhao, H., and Kang, M., 1999, A PDE-Based Fast Local Level Set Method, *Journal of Computational Physics*, **155**, pp.410-438.

[22] Osher, S., and Sethian, J.A., 1988, Fronts Propagating with Curvature-Dependent Speed: Algorithms Based on Hamilton-Jacobi Formulations, *Journal of Computational Physics*, **79**, pp.12-49.

[23] Saurel, R., and Abgrall, R., 1999, A Simple Method for Compressible Multifluid Flows, *SIAM Journal on Scientific Computing*, **21**(3), pp.1115-1145.

[24] Sethian, J.A., 1999, Level Set Methods and Fast Marching Methods, *Cambridge University Press*.

[25] Shu, C.-W., and S. Osher, S., 1989, Efficient Implementation of Essentially Non-Oscillatory Shock-Capturing Schemes II (two), *Journal of Computational Physics*, **83**, pp.32-78.

[26] van Albada, G.D., van Leer, B., and Roberts, W.W., 1982, A Comparative Study of Computational Methods in Cosmic Gas Dynamics, *Astronomy and Astrophysics*, **108**, pp.76-84.

[27] van Leer, B., 1979, Towards the Ultimate Conservative Difference Scheme, A Second Order Sequel to Godunov's Method, *Journal of Computational Physics*, **32**, pp.101-136.